Combinatorial Approach to Turbine Bond Coat Discovery

Christopher Jason Metting,[†] Jonathan Kenneth Bunn,[†] Ellen Underwood,[†] Stephen Smoak,[†] and Jason Hattrick-Simpers*,[†]

[†]SmartState Center for Strategic Approaches to the Generation of Electricity, Department of Chemical Engineering, University of South Carolina, Columbia, South Carolina 29208, United States

S Supporting Information

ABSTRACT: A nondestructive method for the high-through-put screening of novel bond coat materials has been developed. By using a suite of characterization techniques, including Raman spectroscopy, fluorescence spectroscopy, and X-ray diffraction, a rapid determination of thermally grown oxide phases and their protective capability over a continuous composition spread sample can be obtained. The methodology is validated with the Ni−Al system. The procedure developed in this work results in the rapid identification of bond coat composition regions in which the preferred thermally grown

oxide, α-Al_2O_3, is nucleated thus significantly reducing the amount of phase space that needs to be explored in subsequent studies.

KEYWORDS: high-throughput, Ni−Al, bond coats, corrosion, thin fims
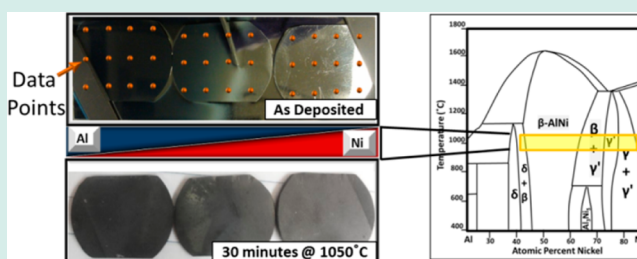
INTRODUCTION

Nickel-based superalloys are currently the most utilized materials for gas turbine blades in both jet turbines and power plants.[1] These systems operate at high temperatures and in extreme environments that can quickly corrode and weaken the blades.[2] To protect the superalloy from both oxidation and thermal damage, a layered coating is applied.[3] The upper layer is a highly porous ceramic, such as yttria-stabilized zirconia, which is used to reduce the effective operating temperature of the turbine base alloy and is referred to as a thermal barrier coating (TBC).[3] Between the TBC and the turbine blade a bond coat layer, generally a (Ni,Pt)-Al alloy or MCrAlY (where M is a transition metal), is deposited to both protect the turbine blade from oxidation and promote adhesion of the combined metal-oxide superstructure.[4,5]

Typically for applications involving exposure to temperatures exceeding 1000 °C the bond coat is engineered to preferentially form an α-Al_2O_3 thermally grown oxide (TGO), because of its parabolic growth rate and high thermodynamic stability to moisture as compared to other oxides such as Cr_2O_3, NiO, and $NiAl_2O_6$.[6,7] Therefore, one of the primary mechanisms for improving the lifetime of the bond coat and, thus, the turbine itself is by promoting the exclusive formation of Al_2O_3.[8]

During the initial oxide growth there is a competition between the nucleation of a host of possible oxides including Al_2O_3, NiO, and $NiAl_2O_6$. Once Al_2O_3 begins to grow a sequential phase evolution follows. The Al_2O_3 forms by first nucleating metastable γ-Al_2O_3 and θ-Al_2O_3 at low temperatures and then transitioning to the more stable hexagonal α-Al_2O_3 phase above 1000 °C.[9−11] Transition from γ,θ-Al_2O_3 to α-Al_2O_3 is accompanied by a significant decrease (∼5%) in

volume, leading to stresses in the TGO that are relieved through void formation.[12,11] These voids, thermal mismatch, diffusion of contaminants, aluminum depletion from the bond coat layer, and continuous growth of the TGO all lead to spallation of the TGO and the TBC.[3] Materials suitable for bond coat applications must exhibit preferential, and preferably excusive, α-Al_2O_3 at the bond coat/thermal barrier coating interface

Currently, β-(Ni,Pt)Al and MCrAlY alloys are being used as bond coat layers in modern turbines.[6] In more recent work in (Ni,Pt)Al alloys, the focus has shifted from the β-(Ni,Pt)Al phase region to the γ/γ'-(Ni,Pt)Al phase region (see Figure 1 for the binary Ni−Al phase diagram), as the latter have been found to form a much more robust α-Al_2O_3 TGO.[13] Even Pt heavy α-(Ni,Pt)Al is also being investigated for potentially improved α-Al_2O_3 formation.[14] These findings have sparked interest in expanding the search for novel bond coat materials that form TGO with superior stability and corrosion resistance properties. This search is complicated, however, by the complex interdependency of the growth of the appropriate TGO with alloy composition, microstructure, interactions with the substrate, and the large range of possible alloying elements.

Previous work has focused on the study of single alloy composition samples, which is a long process for such compositionally complicated systems. Materials scientists confronted with the need to systematically investigate large phase spaces have increasingly turned to high-throughput
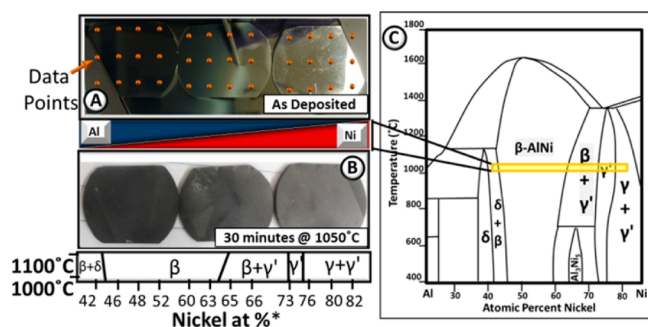
Figure 1. Bond coat composition spread on Inconel 600 substrate. (A) Ni−Al composition spread deposited after preheating at 500 °C for 30 min. Orange dots mark where data was taken. The full temperature profile can be found in the Supporting Information. (B) After 30 min at 1050 °C. (C) Ni−Al phase diagram with the deposited composition region at 1050 °C. (% Composition based on EDS results)[24].

methodologies.[15−21] In this approach, a large number of samples are simultaneously formed, processed, and subsequently characterized for their figure of merit by utilizing parallel or serial measurement techniques. Methods for the design of thin-film combinatorial libraries covering substantial portions of the ternary and quaternary phase diagrams have been well documented in the literature.[22,16,23] To this moment, however, there are no examples of methodologies for determining the high-temperature oxidation properties of combinatorial libraries despite the importance of such materials to a host of defense, transportation, and energy applications.

In this work, we demonstrate the development of a novel combinatorial method for mapping oxide phase growth regions as well as evaluating the underlying bond coat metal during temperature cycling. The goal of this work is to delineate a nondestructive suite of characterization techniques, which will expedite the initial identification of novel bond coat materials that preferentially grow the desired Al_2O_3 scale. Here, we have focused on the Ni−Al system as an elementary proof-of-principle with the understanding that the methodologies developed here can readily be extended to the more complicated MCrAlY group of materials.

■ EXPERIMENTAL PROCEDURES

Polycrystalline alloy 600 Inconel was used as a representative turbine material. The material was purchased from HPAlloy, Inc. as a 0.037″ thick × 11.937″ × 12″ sheet. A 1−1/8″ hole saw from Bosch was used to cut tokens from the sheet. The tokens were mechanically polished down to a 1 μm grit and sheared on either side so as to fit into a 2.54 cm outer diameter quartz tube.

The prepared tokens were mounted as shown in Figure 1A on top of a glass reference slide and placed in an AJA 5-gun sputtering system. The glass reference slide was used to characterize the as-deposited microstructure of the Ni−Al films without diffraction peaks from the substrate, determine composition using energy dispersive spectroscopy (EDS), and calibrate the film thickness. The results from this reference slide were used to assist in interpreting the diffraction patterns from the Ni−Al films on the Inconel substrate. The samples were aligned so that the sheared sides of the tokens were parallel to the composition spread direction. The orientation of the composition gradient is pictorially represented between Figures 1A and 1B. The system was evacuated to a base pressure of 1.4 × 10⁻⁸ Torr. Because the Ni−Al coatings did not exhibit good

adhesion to the Inconel at higher nickel concentrations when deposited at room temperature, the substrate stage was heated to 500 °C immediately prior to deposition to promote nucleation and adhesion of the film to the Inconel substrate. The sputtering system configuration prevented continuous heating of the sample during deposition. Once the substrate had reached the temperature, as indicated by the heating stage thermocouple, the substrate heater was turned off, the stage was moved into the aforementioned orientation, and the deposition was initiated. The temperature profile for the tokens during the deposition as a function of time is provided in the Supporting Information, Figure S6.

The composition spread was created by simultaneously depositing Ni and Al single element targets (from Kurt J. Lesker Company) for 121 min in a 5 mTorr Ar atmosphere. Ni was deposited at 190 W using a RF power supply, and Al was deposited at 100 W using a direct current (DC) power supply, producing a film with an average thickness of 1 μm (validated using a Tencor Alphastep 200 profilometer). Thickness measurements at multiple data points are provided in the Supporting Information, Figure S7.

For the oxidation studies, the samples were cycled 4 times in a Carbolite 2.54 cm outer diameter (OD) quartz tube furnace under atmosphere at 1050 °C for cumulative times of 5, 10, 20, and 30 min and transferred to a perforated Inconel tray for an air quench to room temperature. Between each heat treatment, the sample was characterized using Raman spectroscopy, fluorescence, and grazing incidence X-ray diffraction (GIXRD). Figure 1B shows the samples after heat treatment for 30 min. The image shows visible regional differences in the oxidized film. The most notable difference is in the middle token where the transition from β to β/γ' is predicted to occur according to the phase diagram at 1050 °C (Figure 1). The sample appears green in the region identified by the phase diagram as β, while in the region identified as β/γ' the sample is gray.

Both Raman and fluorescence spectra were taken on a Horiba Olympus spectroscopy system using a 50× objective and a spot size of 1.03 μm. Spectra were taken using both a 441.6 nm blue laser and 632.8 nm red laser. Because Raman scattering is relative to the excitation wavelength whereas fluorescence occurs at a fixed wavelength, changing the probing wavelength changes the peak position of the Raman signal in absolute wavelength. Taking spectra with multiple probing wavelengths reduces the chances of overlapping the Raman signal and the fluorescence seen in Figure 2. On each token a total of 12 points were measured using an evenly distributed 3 × 4 grid across the entire token (the orange markers in Figure 1A). Four compositions were measured on each wafer. Three points were measured for each composition to ensure reproducibility of the spectra and to investigate the potential effect of nonuniform quenching across the token. The compositional gradient direction and data point markers were scribed to ensure that the same points were sampled after each temperature treatment. GIXRD measurements were taken on a Rigaku Ultima IV using a 2 mm front-end slit to limit the probed surface area. With the GIXRD geometry, diffraction was obtained by averaging over the points of constant composition, providing 4 diffractograms per token.

Elemental compositions were determined by an FEI Quanta 200 SEM EDS. Many of the phase regions were distinguishable through visual inspection and correspond with the theoretical
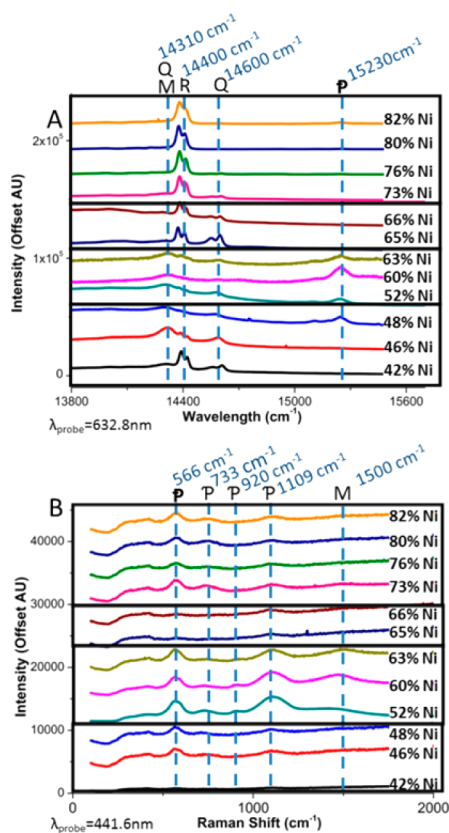
Figure 2. Spectroscopy for the 5 min heat treatment at 1050 °C using (A) 632.8 nm and (B) 441.6 nm lasers. M: NiO 1-Magnon Raman, P: NiO 1-Phonon Raman, Q: Q1,Q2 θ-Al_2O_3 Fluorescence, p: NiO 2-Phonon Raman, and R: R1, R2 α-Al_2O_3 Fluorescence.

phases indicated by EDS results and the Ni−Al binary phase diagram as shown in Figure 1.

RESULTS AND DISCUSSION

The composition spreads on both the Inconel tokens and the glass slide were characterized prior to heat treatment. GIXRD analysis of a glass reference slide showed that the section of the sample between 46% and 63% nickel exhibited diffraction peaks consistent with a mixture of β-NiAl and γ'-NiAl rather than the expected pure β-NiAl, and the 76% to 82% nickel region only showed γ'-NiAl rather than the expected γ/γ'-NiAl. Much longer count times were needed to observe diffraction patterns from the 76% to 82% nickel region indicating that the material was weakly crystalline after deposition. No peaks for the low temperature peritectic Ni_5Al_3 phase were detected as well. These results indicate that the cooling profile experienced by the sample resulted in the formation of nonequilibrated structures across the binary composition spread and in the future the effect of alternative postsample processing will be investigated.

Since the rapid formation of α-Al_2O_3 on the surface of the metal is the baseline figure of merit for the capability of a bond coat to resist rapid oxidation, we took advantage of the high sensitivity of fluorescence to the presence of aluminum oxide as our initial screen. After each oxidation treatment, fluorescence was used to characterize trends in the Al_2O_3 scale formation by monitoring peaks for the $^2E\rightarrow^4A_2$ energy transition (R in Figure 2) resulting from α-Al_2O_3 phase and the doublet at ~14550 cm^{-1} and ~14500 cm^{-1} corresponding to the θ-Al_2O_3

phase(Q in Figure 2).[25,26] The doublet corresponding to the α-Al_2O_3 was observed to be shifted from the position expected for pure, unstressed ruby $^2E\rightarrow^4A_2$ transitions, which is common for scale forming Al-containing alloys.[27] There are many possible contributions to this shift, including residual stresses, concentration of Cr and other contaminants, and temperature.[26,28,29] Some of the measurements also show a broad fluorescence at ~14000 cm^{-1} and a peak at ~14300 cm^{-1}, which may be correlated to a γ-$Al_2O_3\rightarrow\theta$-Al_2O_3 phase transformation.[26] When the peak at ~14300 cm^{-1} is strongly present, the θ-Al_2O_3 doublet appears as a single peak at ~14580 cm^{-1}, which has been observed by others in oxide scales formed on (111)NiAl.[26]

For alumina to fluoresce, Cr ions must be present. Although it is not clear whether the Cr in this system originated from the sputtering targets (the Al target Cr impurity is <0.3 ppm by wt. and the Ni target Cr impurity is 1.6 ppm by wt.) or diffusion from the Inconel substrate, there were no fluorescence peaks that would indicate the Cr concentration was high enough to exhibit Cr−Cr interactions.[28,30]

To reduce the overlap between the Al_2O_3 fluorescence and the Raman signal, a 441.6 nm blue laser was used to obtain Raman spectra absent of the Al_2O_3 fluorescence. Although no Raman peaks attributable to Al_2O_3 were observed for any of the samples, the NiO 1-phonon mode at 566 cm^{-1}, the NiO 2-phonon modes at 733 cm^{-1}, 920 cm^{-1}, and 1109 cm^{-1}, and the NiO 2-magnon mode at 1500 cm^{-1} were all observed.[31,32]

XRD is a routinely used characterization technique for determining the crystallographic phases of a material. In GIXRD the incoming X-ray beam is fixed at $\theta = $ ~1° and the 2θ scattering geometry is maintained by the angle of the detector arm. This geometry helps limit scattering from the substrate and increase the instrument's sensitivity to surface material, in this case the bond coat and the TGO. Although this technique provided a wealth of data, similarities in composition and crystal structure between the bond coat, the Inconel substrate, and the surface oxides made conclusive indexing of the diffractograms difficult as many of the major peaks in this particular system reside at very similar 2θ values (Figure 3). Still, key information was obtained about the bond coat and substrate oxidation as well as the initial bond coat phases.
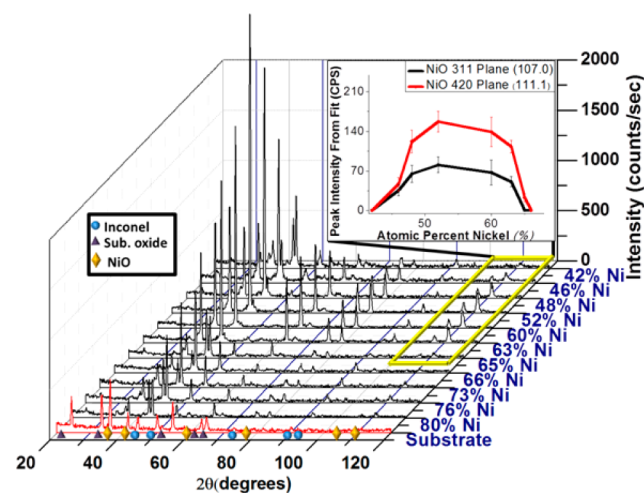
Figure 3. XRD results for the 5 min heat treatment at 1050 °C. All peaks were indexed. Prevalent peaks are labeled. (inset) Peak intensity of two NiO diffraction peaks from peak fitting.

The combination of fluorescence, Raman, and GIXRD results can be used to determine information about the oxide formation as a function of nickel composition. Figure 2 shows the combined spectroscopic results for a 5 min heat treatment at 1050 °C. The bold black lines in Figure 2 indicate four regions with similar characteristics and are in the following nickel compositions: 42% to 48%, 52% to 63%, 65% to 66%, and 73 to 82%. Interestingly, the 52%-66% Ni region, corresponding to primarily β-NiAl phase region at 1050 °C, exhibited primarily NiO growth rather than Al_2O_3. It should be pointed out that the diffraction peaks for $NiAl_2O_4$, another competing oxide, are not observed in the data. This indicates $NiAl_2O_4$ is not a majority oxide phase. The presence of NiO is observed at all oxidation times by both Raman and GIXRD. The inset in Figure 3 shows the fitted peak intensity for two diffraction peaks, which can be exclusively attributed to NiO, as a function of composition and clearly demonstrates strong NiO growth in this compositional region.

The growth of NiO on a material deposited in the nominal β-NiAl composition region is notable and is explained by the GIXRD results from the reference slide. The film after deposition is composed of a nonequilibrium mixture of β-NiAl and γ'-NiAl rather than a single phase alloy. The distribution of the phases through the film thickness is unknown at this moment and will be investigated in future detailed SEM/TEM studies; however, the presence of γ'-NiAl in the mixed phase could promote the nucleation of NiO, which has been previously reported.[33] A similar study that involved nonheat treated Ni−Al composition spreads exhibited significant α-Al_2O_3 and θ-Al_2O_3 fluorescence in the β-NiAl region (Supporting Information, Figure 5S) indicating that the heat treatment inhibited α-Al_2O_3 formation in the β-NiAl region for this study. Thus the heating pretreatment, while necessary for promoting adhesion across the entire composition spread, perturbs the phase and possibly surface composition of the films, inhibiting growth of the appropriate oxide. Further studies are currently under way to understand and to control the film microstructure.

The 65%-66% Ni region, corresponding to the β/γ' NiAl phase region at the oxidation temperature, showed almost exclusive Al_2O_3 oxide with no discernible NiO diffraction peaks (Figure 3) and only a small NiO Raman signal (Figure 2). This region also exhibits significant fluorescence signal corresponding to the metastable Al_2O_3 phases (Figure 2) during early temperature treatments, which then transform to the stable α-Al_2O_3 over time (Figure 4). The reduced α-Al_2O_3 fluorescence peak intensity in Figure 4A after 30 min is most likely due to spallation of the TGO, which was also observed optically.

The 73%-82% Ni region corresponding to the γ'-NiAl and the γ/γ'-NiAl phase region show some NiO Raman signal (Figure 2) and diffraction peaks (Figure 4); however, the signal is far less intense than that seen in the β-NiAl, and the large α-Al_2O_3 fluorescence signal indicates that α-Al_2O_3 is the primary oxide formed. The fluorescence corresponding to metastable Al_2O_3 is weak, even at the 5 min heat treatment, which may imply a faster transition to the α-Al_2O_3 phase occurred in this region than that seen in the β/γ'-NiAl region.

Even with the short temperature treatments, the combination of small film thickness and substrate stresses due to substrate bowing during the quenching procedure caused spallation after just 5 min. The oxidation of the substrate was tracked using diffraction peaks corresponding exclusively to substrate oxide formation (Figure 5). The present work focused primarily on
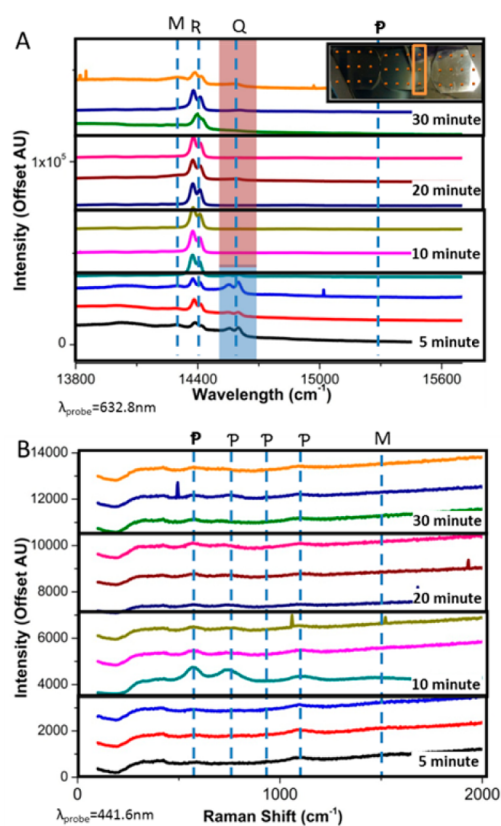

Figure 4. Spectroscopy for the temperature dependence of the 66 at.% nickel composition using (A) 632.8 nm and (B)441.6 nm lasers. M: NiO 1-Magnon Raman, P: NiO 1-Phonon Raman, Q: Q1,Q2 θ-Al_2O_3 Fluorescence, p: NiO 2-Phonon Raman, and R: R1, R2 α-Al_2O_3 Fluorescence. The blue region shows significant metastable Al_2O_3 fluorescence while the red does not, illustrating the transformation of metastable Al_2O_3 to stable α-Al_2O_3.
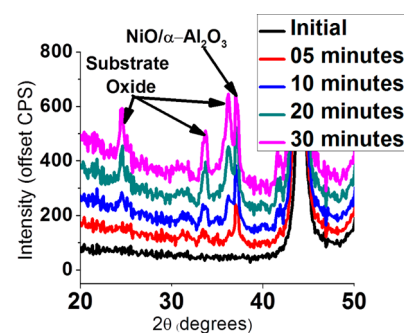
Figure 5. XRD for the 66 at.% nickel for different temperature treatments. Growth of the substrate oxide is evident from the diffraction.

initial oxide formation; however, tracking the substrate oxide diffraction peak can be used in future work to study the protective capabilities of different bond coat compositions.

The results of this study are summarized in Figure 6. Although the GIXRD provided phase information about the oxide formation on the bond coat surface, the similarities between the crystal structures of the bond coat, the substrate, and their oxides made the resulting patterns difficult to interpret. Therefore, the Raman and fluorescence data were imperative to both obtain information about the TGO growth
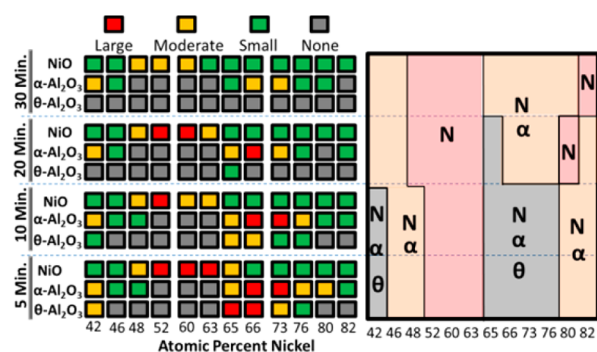
Figure 6. Schematic depicting trends in oxide formation based on the Raman, Fluorescence, GIXRD. The NiO trends are primarily obtained from GIXRD. The Al_2O_3 trends are obtained from luminescence. 'α' stands for α-Al_2O_3, "θ" stands for θ-Al_2O_3, and "N" stands for NiO. The data used to obtain this figure is presented in Supporting Information, Figures S1–S4.

that could not be determined by GIXRD and to validate the observation of the NiO and substrate oxide growth

With all three characterization techniques, surface averaged information about NiO and the Al_2O_3 phases present during oxidation were obtained. Results are in agreement with each other and have indicated that the higher Ni composition alloys preferentially formed Al_2O_3. The Al_2O_3 formation in the γ/γ'-NiAl region at early times is commensurate with literature and is one of the reasons for current interest in Pt stabilized γ/γ'-NiAl as a bond coat material.[6,8,13,34]

CONCLUSION

A methodology has been developed for the high-throughput screening of novel bond coat materials. A suite of non-destructive characterization techniques has been demonstrated to track the quality and phase of oxide scales formed on bond coat materials as a function of bond coat composition over time. Fluorescence was utilized to track Al_2O_3 phases, Raman spectroscopy provided information about the nickel oxide content, and XRD measured the protection capabilities of the bond coat by tracking the substrate oxide growth as well as initial bond coat phase.

The process and characterization techniques used in this work can be directly applied to a variety of substrates and bond coat compositions ((Ni,Pt)Al, MCrAlY, etc.) as well as more novel bond coat systems. By using longer deposition times, thicker bond coat films can be fabricated to study long-term TGO growth and spallation. The benefit of this technique is that it allows for the rapid screening of different coatings on various substrates and heat treatments to identify which regions nucleate the desired TGO. Once the most promising regions are identified, targeted, time intensive studies of the specific roles of substrate/bond coat interdiffusion and long-term adhesion can be undertaken.

ASSOCIATED CONTENT

Ⓢ Supporting Information

Figures S1–S4 contain select data used to produce the summary in Figure 6. Figure S5 shows results for a similar study for a sample that was not heat treated prior to oxidation. Figure S6 shows the temperature profile of the sample substrate during Ni–Al deposition. Figure S7 shows profilometery results for multiple points along the composition gradient. This material is available free of charge via the Internet at http://pubs.acs.org.

AUTHOR INFORMATION

Corresponding Author

*E-mail: simpers@cec.sc.edu.

Author Contributions

The manuscript was written through contributions of all authors. All authors have given approval to the final version of the manuscript.

Notes

The authors declare no competing financial interest.

REFERENCES

(1) Reed, R. C. *The Superalloys: Fundamentals and Applications*; Cambridge University Press: Cambridge, U.K., 2006; p 372.

(2) Lai, G. Y. *High-Temperature Corrosion and Materials Applications*; ASM International: Materials Park, OH, 2007; p 461.

(3) Clarke, D. R.; Levi, C. G. Materials Design for the Next Generation Thermal Barrier Coatings. *Annu. Rev. Mater. Res.* **2003**, *33*, 383–417.

(4) Gandy, D.; Shingledecker, J.; Viswanathan, R. Advances in Materials Technology for Fossil Power Plants. In *Proceedings from the Sixth International Conference*, Santa Fe, New Mexico, August 31–September 3, 2010; ASM International: Materials Park, OH, 2011.

(5) Wu, R. T.; Reed, R. C. On the Compatibility of Single Crystal Superalloys with a Thermal Barrier Coating System. *Acta Mater.* **2008**, *56*, 313–323.

(6) Hou, P. Y. Segregation Behavior at TGO/Bondcoat Interfaces. *J. Mater. Sci.* **2008**, *44*, 1711–1725.

(7) Pint, B.; More, K. L. Characterization Of Alumina Interfaces in TBC Systems. *J. Mater. Sci.* **2009**, *44*, 1676–1686.

(8) Gleeson, B.; Mu, N.; Hayashi, S. Compositional Factors Affecting the Establishment and Maintenance of Al_2O_3 Scales on Ni–Al–Pt Systems. *J. Mater. Sci.* **2009**, *44*, 1704–1710.

(9) Yang, J.; Schumann, E.; Levin, I. Transient Oxidation of NiAl. *Acta Mater.* **1998**, *46*, 2195–2201.

(10) Pettit, F. S. Oxidation Mechanisms for Nickel-Aluminum Alloys at Temperatures Between 90 and 1300 °C. *Trans. Metal. Soc. AIME* **1967**, *239*, 1296.

(11) Hou, P.; Paulikas, A.; Veal, B. W. Stress Development and Relaxation In Al_2O_3 During Early Stage Oxidation Of NiAl. *Lawrence Berkeley Lab.* **2005**, *33*, 535–543.

(12) Hou, P. Y. Segregation Phenomena at Thermally Grown Al_2O_3/Alloy Interfaces. *Annu. Rev. Mater. Res.* **2008**, *38*, 275–298.

(13) Hayashi, S.; Wang, W. Interdiffusion behavior of Pt-modified γ-Ni+γ'-Ni_3Al alloys coupled to Ni-Al-based alloys. *Metall. Mater.* **2005**, *36*, 1769–1775.

(14) Hayashi, S.; Ford, S. I.; Young, D. J.; Sordelet, D. J.; Besser, M. F.; Gleeson, B. α–NiPt(Al) and Phase Equilibria In The Ni–Al–Pt System at 1150 °C. *Acta Mater.* **2005**, *53*, 3319–3328.

(15) Hunter, D.; Osborn, W.; Wang, K.; Kazantseva, N.; Hattrick-Simpers, J.; Suchoski, R.; Takahashi, R.; Young, M. L.; Mehta, A.; Bendersky, L. A.; Lofland, S. E.; Wuttig, M.; Takeuchi, I. Giant Magnetostriction In Annealed $Co_{(1-x)}Fe_{(x)}$ Thin-Films. *Nat. Commun.* **2011**, *2*, 518.

(16) Cui, J.; Chu, Y. S.; Famodu, O. O.; Furuya, Y.; Hattrick-Simpers, J.; James, R. D.; Ludwig, A.; Thienhaus, S.; Wuttig, M.; Zhang, Z. Y.; Takeuchi, I. Combinatorial Search of Thermoelastic Shape-Memory Alloys with Extremely Small Hysteresis Width. *Nat. Mater.* **2006**, *S1*, 557–631.

(17) Scheidtmann, J.; Weiss, P. A.; Maier, W. F. Hunting for Better Catalysts and Materials-Combinatorial Chemistry and High Throughput Technology. *Appl. Catal., A* **2001**, *222*, 79−89.

(18) Svedberg, E. B.; Van de Veerdonk, R. J. M.; Howard, K. J.; Madsen, L. D. Quantifiable Combinatorial Materials Science Approach Applied to Perpendicular Magnetic Recording Media. *J. Appl. Phys.* **2003**, *93*, 5519−5526.

(19) Takeuchi, I.; Van Dover, R. B.; Koinuma, H. Combinatorial Synthesis and Evaluation of Functional Inorganic Materials Using Thin-Film Techniques. *MRS Bull.* **2002**, *27*, 301−308.

(20) Zhao, J. C. Combinatorial Approaches as Effective Tools in the Study of Phase Diagrams and Composition-Structure-Property Relationships. *Prog. Mater. Sci.* **2006**, *51*, 557−631.

(21) Maier, W. F.; Stowe, K.; Sieg, S. Combinatorial and High-Throughput Materials Science. *Angew. Chem., Int. Ed.* **2007**, *46*, 6016−6067.

(22) Zarnetta, R.; Takahashi, R.; Young, M. L.; Savan, A.; Furuya, Y.; Thienhaus, S.; Maass, B.; Rahim, M.; Frenzel, J.; Brunken, H.; Chu, Y. S.; Srivastava, V.; James, R. D.; Takeuchi, I.; Eggeler, G.; Ludwig, A. Identification of Quaternary Shape Memory Alloys with near-Zero Thermal Hysteresis and Unprecedented Functional Stability. *Adv. Funct. Mater.* **2010**, *20*, 1917−1923.

(23) Hattrick-Simpers, J. R.; Hunter, D.; Craciunescu, C. M.; Jang, K. S.; Murakami, M.; Cullen, J.; Wuttig, M.; Takeuchi, I.; Lofland, S. E.; Benderksy, L.; Woo, N.; Dover, R. B. V.; Takahashi, T.; Furuya, Y. Combinatorial Investigation of Magnetostriction in Fe-Ga and Fe-Ga-Al. *Appl. Phys. Lett.* **2008**, *93*, 102507.

(24) Okamoto, H. Al-Ni (Aluminum-Nickel). *J. Phase Equilib. Diffus.* **2004**, *25*, 394−394.

(25) Sturge, M. D. Effect of a Static Electric Field on the R Lines of (3d) s Ions in Corundum. *Phys. Rev. B* **1964**, *133*, A795.

(26) Wen, Q.; Lipkin, D. Luminescence Characterization of Chromium Containing theta Alumina. *J. Am. Ceram. Soc.* **1998**, *48*, 3345−3348.

(27) Lipkin, D.; Clarke, D. R. Measurement of the stress in oxide scales formed by oxidation of alumina-forming alloys. *Oxid. Met.* **1996**, *45*, 267−280.

(28) Yu, H. Effect of Codoping on the R-Line Luminescence of Cr^{3+}-Doped Alumina. *J. Am. Ceram. Soc.* **2002**, *70*, 1966−1970.

(29) Margueron, S. H.; Clarke, D. R. Stress anisotropy of the R-line luminescence lifetime in single crystal Cr-doped sapphire (ruby). *J. Appl. Phys.* **2007**, *101*, 093521.

(30) Sohn, Y.; Vaidyanathan, K.; Ronski, M. Thermal Cycling of EB-PVD/MCrAlY Thermal Barrier Coatings: II. Evolution of Photo-Stimulated Luminescence. *Surf. Coat. Technol.* **2001**, *147*, 102−109.

(31) Merlin, R.; Weber, W. *Raman Scattering in Materials Science*; Springer: Berlin, Germany, 2000; p 492.

(32) Mironova-Ulmane, N.; Kuzmin, A.; Steins, I.; Grabis, J.; Sildos, I.; Pärs, M. Raman Scattering in Nanosized Nickel Oxide NiO. *J. Phys.: Conf. Ser.* **2007**, *93*, 012039.

(33) Velon, A.; Olefjord, I. Oxidation Behavior of Ni_3Al and Fe_3Al: II. Early Stage of Oxide Growth. *Oxid. Met.* **2001**, *56*.

(34) Zhang, Y.; Pint, B. A.; Haynes, J. A.; Wright, I. G. A platinum-enriched $\gamma+\gamma'$ two-phase bond coat on Ni-based superalloys. *Surf. Coat. Technol.* **2005**, *200*, 1259−1263.